7-2016

Reactive flow modeling of small scale detonation failure experiments for a baseline non-ideal explosive

David E. Kittell
Purdue University

Nick R. Cummock
Purdue University

Steven F. Son
Purdue University, sson@purdue.edu

Recommended Citation
D. E. Kittell, N. R. Cummock, and S. F. Son, "Reactive Flow Modeling of Small Scale Detonation Failure Experiments for a Baseline Non-ideal Explosive," Journal of Applied Physics Letters, Vol. 120(6), p. 064901, 2016. http://dx.doi.org/10.1063/1.4959818

Reactive flow modeling of small scale detonation failure experiments for a baseline non-ideal explosive

David E. Kittell, Nick R. Cummock, and Steven F. Son

Citation: Journal of Applied Physics **120**, 064901 (2016);
View online: https://doi.org/10.1063/1.4959818
View Table of Contents: http://aip.scitation.org/toc/jap/120/6
Published by the American Institute of Physics

JOURNAL OF APPLIED PHYSICS **120**, 064901 (2016)

Reactive flow modeling of small scale detonation failure experiments for a baseline non-ideal explosive

David E. Kittell, Nick R. Cummock, and Steven F. Son
School of Mechanical Engineering, Purdue University, West Lafayette, Indiana 47907, USA

(Received 28 March 2016; accepted 13 July 2016; published online 8 August 2016)

Small scale characterization experiments using only 1–5 g of a baseline ammonium nitrate plus fuel oil (ANFO) explosive are discussed and simulated using an ignition and growth reactive flow model. There exists a strong need for the small scale characterization of non-ideal explosives in order to adequately survey the wide parameter space in sample composition, density, and microstructure of these materials. However, it is largely unknown in the scientific community whether any useful or meaningful result may be obtained from detonation failure, and whether a minimum sample size or level of confinement exists for the experiments. In this work, it is shown that the parameters of an ignition and growth rate law may be calibrated using the small scale data, which is obtained from a 35 GHz microwave interferometer. Calibration is feasible when the samples are heavily confined and overdriven; this conclusion is supported with detailed simulation output, including pressure and reaction contours inside the ANFO samples. The resulting shock wave velocity is most likely a combined chemical-mechanical response, and simulations of these experiments require an accurate unreacted equation of state (EOS) in addition to the calibrated reaction rate. Other experiments are proposed to gain further insight into the detonation failure data, as well as to help discriminate between the role of the EOS and reaction rate in predicting the measured outcome. *Published by AIP Publishing.* [http://dx.doi.org/10.1063/1.4959818]

I. INTRODUCTION

Non-ideal explosives, such as ammonium nitrate plus fuel oil (ANFO), are challenging to characterize because of the wide range of the parameter space in sample composition, density, and microstructure. There exists a strong need for the screening, characterization, and modeling of non-ideal explosives; both in the mining industry to tailor the fracture and heaving processes for rocks,[1] as well as national security to more adequately assess the threat from home-made explosives (HMEs).[2] Slight modifications to a non-ideal explosive may have dramatic effects on the sensitivity to initiation and the detonation performance. For example, pre-compressing ANFO beyond $\sim$1.4 g/cm^3 may result in initiation failure, owing to the dead-pressing phenomenon.[3] In addition, ammonium nitrate prill size and porosity may result in ANFO detonation velocities ranging between 1.5 and 4.0 km/s, owing to different levels of fuel oil absorption within the prills[4,5] or other factors. A broad spectrum of non-ideal behavior may be observed in shock front curvature,[6] diameter effects,[7] and interactions with confining material,[8] which cannot be determined without large scale (currently $\sim$1 kg or greater) rate stick tests.[6,8]

The wide range of non-ideal explosives prohibits large scale characterization of every composition of interest. Previous attempts to develop small scale characterization tests (e.g., Floret,[9] mushroom,[10] and tiny plate[11] tests) relied on high explosives that can sustain a detonation wave with only a few grams of material. These small scale tests are not applicable in the same way for non-ideal explosives, which exhibit long reaction zones (up to a few cm) and large critical diameters, below which a detonation will not steadily propagate. It is largely unknown in the scientific community whether any useful or meaningful result may be obtained from small scale characterization data for non-ideal explosives, and also if a minimum sample size or level of confinement exists for the tests. In addition, no previous work has shown if a reactive flow model, such as ignition and growth,[12] is relevant for simulating some or all of the small scale experimental data on non-ideal explosives.

In this work, a small scale characterization experiment utilizing a 35 GHz microwave interferometer (MI) is considered following the development by Janesheski *et al.*[2] and Kittell *et al.*[13] Microwave interferometry (MI) is a non-intrusive technique with a high temporal resolution, and is used to measure the instantaneous shock or detonation velocity in explosives. Specifically, this technique records the phase and amplitude of microwave signals that are transmitted through an unreacted explosive and reflected back at dielectric discontinuities, such as a shock wave or reaction front.[14,15] In the present study, explosive-filled waveguides are used to propagate only the lowest microwave mode through an optically transparent media. An explosive booster is used to initiate samples of ANFO, where the confiner (i.e., waveguide) wall thickness and sound speed are varied to tailor the behavior of the shock velocity profile corresponding to detonation failure.

The objective of the work is to determine if a reactive flow model based on the theory of ignition and growth[12] is relevant to the small scale MI experiments, and whether the obtained shock velocity data may be used to calibrate model parameters (i.e., reaction rate, equation of state (EOS), or otherwise). To this end, four different experimental configurations each requiring 1–5 grams of a baseline ANFO

TABLE I. Summary of four charge configurations. Also shown are the material wavelengths for Primasheet® 1000 (λ_1) and ANFO (λ_2).

Abbr.	I.D. (mm)	Conf. material	t_w (mm)	λ_1 (mm)	λ_2 (mm)
SM	6.52	304 Stainless steel	0.7	5.80	5.91
THN	11.28	304 Stainless steel	0.7	5.34	5.42
PVC	11.28	304 stainless steel	0.7	5.34	5.42
		PVC outer layer	19.1		
THK	11.28	304 Stainless steel	32.5	5.34	5.42

explosive are reported as proof of concept and for model calibration. Several model assumptions are made to reduce the number of free parameters, and to retain some physical significance to the parameter values. Overall, the calibrated reactive flow model for ANFO demonstrates the potential of the small scale detonation failure experiments to augment or possibly replace some larger scale explosives tests.

II. EXPERIMENTAL METHODS

The experimental apparatus was similar to one used in previous works.[2,13] In summary, a 35 GHz signal was generated using a custom microwave interferometer and transmitted to the test article through a solid 6.35 mm dia. polytetrafluoroethylene (PTFE) waveguide. Four different test article geometries were considered, refer to Table I and Figs. 1 and 2 for descriptions. A quadrature mixer was used to produce two-channel output 90° out of phase and was recorded using a Tektronix DPO4034 digital phosphor oscilloscope. Timing of the experiment was based on first light observed by fiber optics: an M34L02 Thorlab patch cable with a 600 μm core dia. transmitted light to a DET10A Thorlab photodetector with 1 ns rise time. Triple shielded coaxial cables (Pasternack

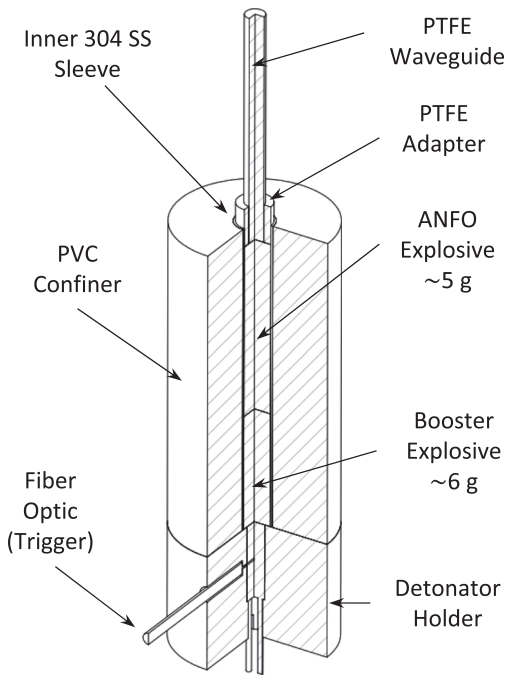

FIG. 1. Cross section of the PVC charge assembly. Refer to Table I for additional details.

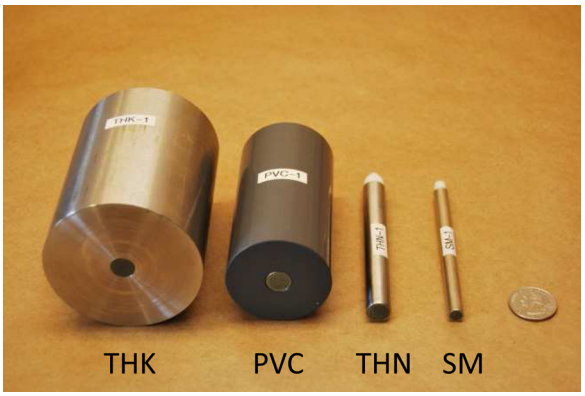

FIG. 2. Different charge geometries and their abbreviations (booster end view). Refer to Table I for additional details.

PE-P195) were used to transmit the photodetector and MI signals from the test cell to the control room; the detonation event was contained inside a thick-walled steel box.

In this study, high explosives were pressed into either 6.52 mm or 11.28 mm dia. stainless steel tubes (i.e., waveguides) for velocity measurement. A Teledyne Risi, Inc., RP-502 detonator was used to initiate a detonation in a 3.81 cm long column of Primasheet® 1000, which transitioned into a 5.72 cm long column of a baseline ANFO explosive. Nylon™ and polyvinyl chloride (PVC) shims were used to achieve nominal pressing increments of 9.53 mm; the target density was 1.44 g/cm^3 for the Primasheet® 1000 booster and 0.826 g/cm^3 for ANFO, corresponding to 98% and 50% of the theoretical maximum density, respectively. The calibrated material wavelength for each explosive and charge geometry is also reported in Table I.

The baseline ANFO formula was a stoichiometric mixture of Kinepouch™ (Orica Mining Services) and 5.32 wt. % diesel fuel, and does not represent a typical ANFO mixture of ammonium nitrate prills. Instead, Kinepouch™ is a blend of crushed ammonium nitrate crystals and some glass micro-balloons for improved shock sensitivity (refer to Fig. 3). The mean particle diameters were estimated to be 60 μm for the ammonium nitrate, and 50 μm for the micro-balloons, based on an image processing analysis of roughly 200 particles. The smallest tube diameter is spanned by at least 100

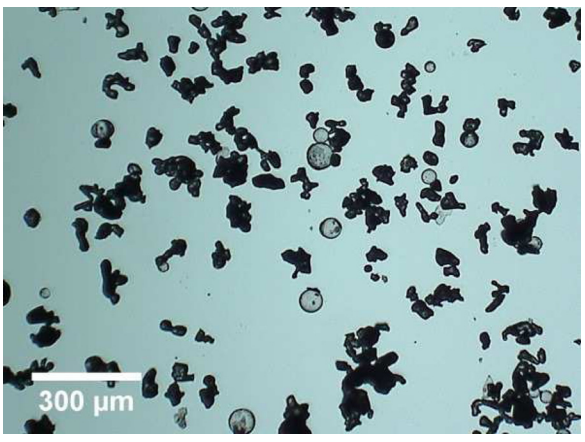

FIG. 3. Microscope image of Kinepouch™ consisting of crushed ammonium nitrate with glass micro-balloons (transparent).

particles; this improves the spatial homogeneity across the test diameter, and allows for more planar shock waves to reflect the MI signal. Unfortunately, no performance data is available for the baseline ANFO formula, as Kinepouch™ is normally mixed with liquid nitromethane. For the present study, nitromethane was found to absorb the microwave radiation and render the MI technique ineffective.

III. MI DATA ANALYSIS

A variety of different analysis techniques may be used to extract a time-resolved shock velocity from the MI output signals.[13] The selection of an analysis technique was made based on the quality of the data obtained, as well as the desired spatial and temporal resolution of the result; for this work, a peak-picking technique was sufficient to process the high quality MI signals (refer to Fig. 4). Spatial resolution was further improved by applying the peak-picking technique to each of the two-channel quadrature signals, and then combining the results.

For the velocity calculations, each advance in phase by 2π corresponds to the advance of the shock wave by one-half wavelength; this also corresponds to the time between consecutive peaks. An average velocity may be calculated between the ith and ith+1 peaks as

$$\bar{v}_i = \frac{\lambda_k/2}{t_{i+1} - t_i}, \tag{1}$$

where λ_k is the calibrated material wavelength from Table I. The material wavelength depends on the microwave frequency, sample diameter, and permittivity, and was calculated in this work using a dynamic calibration. Specifically, the known length of each explosive together with the transition times was used to determine a wavelength and permittivity value from each test; permittivity values were averaged over sixteen different tests, as the sample compositions remained the same.

All MI velocity results are shown in Fig. 5, corresponding to the different geometries in Table I with four repeated measurements in each case. The high level of repeatability

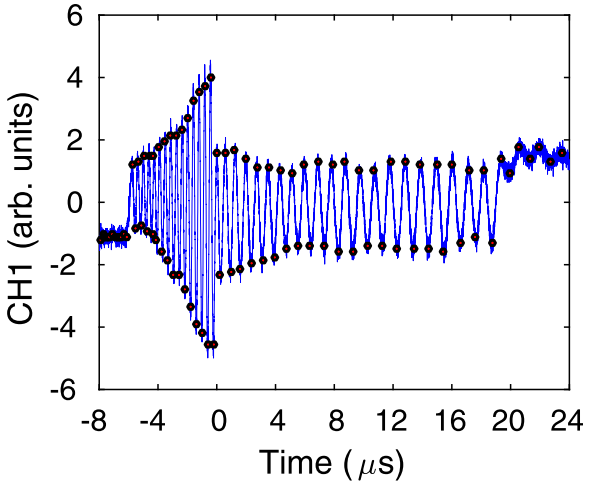

FIG. 4. Example of the MI signal for the PVC experiment; $t = 0$ corresponds to the transition from the booster to ANFO.

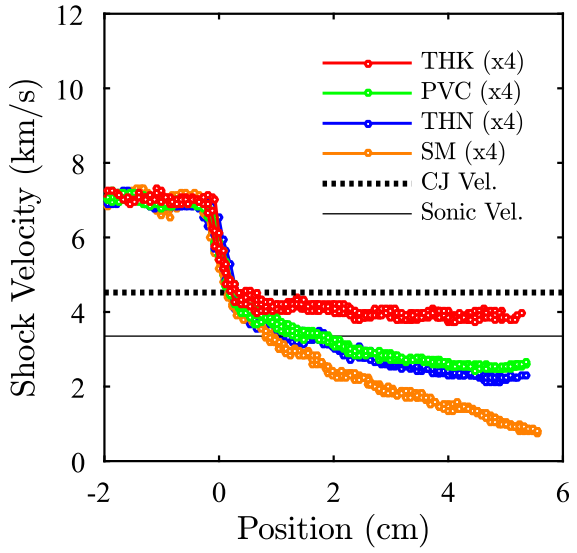

FIG. 5. Shock velocity results for the different configurations in Table I; $x = 0$ corresponds to the transition from the booster to ANFO.

observed in the results is attributed to the tight control of sample density; the standard deviation of the ANFO samples was 0.003 g/cm^3, or 0.4% of the mean density value. In addition, the MI data is plotted together with thermochemical equilibrium calculations from CHEETAH[16] for the Chapman-Jouguet (CJ) detonation velocity ($D_{CJ} = 4.52$ km/s) and the sonic velocity ($a = 3.35$ km/s). Here the sonic velocity, a, corresponds to the fully reacted state assumed from CJ theory. From these values, it is clear that all velocity curves correspond to detonation failure, where the failure rate is influenced by the confinement and charge diameter. The origin of the velocity curves near the CJ value at $x = 0$ is also interesting, as this point is similar (if not equal) across all the levels of confinement and sample diameters tested. Further discussion of the velocity inflection point may be found in the model development and results sections, where it is proposed that the shock velocity at $x = 0$ lies on the unreacted Hugoniot of the ANFO test samples.

IV. MODEL DEVELOPMENT

The reactive flow model used is similar to the original ignition and growth model proposed by Lee and Tarver.[12] Some differences include a Mie-Grüneisen equation of state (EOS) for the unreacted explosive, a phenomenological porosity model to describe void collapse in ANFO, and a set of mixture laws which assumes mechanical and thermal equilibrium. However, the original two-term rate law is retained, with the same burn surface topology and burn rate functions as well.

A. Unreacted equation of state

Beginning with the unreacted EOS, Gruneisen's postulate is assumed to hold[17]

$$\left(\frac{\partial p}{\partial e}\right)_v = \Gamma_0 \rho_0, \tag{2}$$

where the product of the Gruneisen parameter, Γ_0, and initial density, ρ_0, is constant; this is a common approximation found in similar work.[18] The incomplete form in Eq. (2) is integrated to obtain

$$p(v,e) = p_H + \Gamma_0 \rho_0 [e - e_H], \tag{3}$$

where the reference pressure, p_H, and energy, e_H, were chosen as the Hugoniot state. The functions p_H and e_H are determined from empirical data in the form of a quadratic shock-particle velocity relationship[19]

$$U_s = c_0 + s u_p + q {u_p}^2, \tag{4}$$

where U_s and u_p are the shock and particle velocities, respectively.

In assembling the unreacted EOS parameters for this work, no shock state data was available for the baseline ANFO explosive. As an approximation, the contributions of the fuel oil and glass micro-balloons to the EOS were neglected. Even then, limited data was available for porous ammonium nitrate (AN). Dremin *et al.*[20] reported the shock Hugoniot for AN at 0.86 g/cm^3 as $U_s = 2.20 + 1.96 u_p$ km/s; however, the density is fixed, and it is not trivial to extrapolate to other densities. The shock Hugoniot is known with much greater accuracy near the crystal density; thus, the crystalline AN parameters were used and extended with a phenomenological porosity model.

B. Porosity model

The p-α model proposed by Hermann,[21] and later improved by Carroll and Holt[22] achieves some of the correct crushing behaviors at both high and low stresses. This model introduces a distension parameter defined by the density ratio,

$$\alpha = \frac{\rho_M}{\rho}, \tag{5}$$

where ρ_M corresponds to the matrix material, ρ corresponds to the porous material, and both densities are evaluated at the same temperature and pressure. The distension parameter is used to modify the look-up of pressure and energy in the matrix EOS according to the relations

$$p(\rho, T, \alpha) = p_M(\alpha\rho, T)/\alpha \tag{6}$$

and

$$e(\rho, T, \alpha) = e_M(\alpha\rho, T). \tag{7}$$

A phenomenological model is then used to define the crushing history in p-α space, which becomes convolved with time during the simulation.

The crushing history is subdivided into an elastic and compaction region, representing reversible and irreversible crushing behaviors, respectively. For pressures above the crush pressure limit, p_s, the porous and matrix EOS are the same, and $\alpha = 1.0$. For pressures within the compaction region, a second order polynomial for $\alpha(p)$ is assumed

$$\alpha(p) = 1 + (\alpha_0 - 1)\left(\frac{p_s - p}{p_s - p_e}\right)^2, \tag{8}$$

where p_e is the elastic pressure limit and $\alpha_0 = \rho_{M0}/\rho_0$ is the initial value of the distension parameter. Finally, the elastic region is defined implicitly by a variation in sound speed. During the preparation of the ANFO charges, minimal force was required to press the samples to the target density of 50% TMD. Higher densities were also pressed with no apparent elastic relaxation; hence, the elastic pressure limit was set to zero. A default value for the crush pressure was also assumed. However, later studies were more successful matching the MI data when the crush pressure was fitted as follows.

C. Shock impedance matching

One interpretation of the MI shock velocity at $x = 0$ in Fig. 5 is that it is the intersection of left- and right-running Hugoniot curves; i.e., for the detonation products of Primasheet® 1000 and the unreacted ANFO samples, respectively. This analysis appears to be reasonable for at least two reasons: (1) shock impedance matching is independent of the sample diameter, which might explain the common velocity origin point in Fig. 5 and (2) a certain run distance is required before chemical reaction will influence the velocity of shock waves in heterogeneous explosives.[23]

Using an analysis from Cooper,[19] the left-running Hugoniot of the detonation products is approximated by the empirical curve fit

$$\hat{P} = 2.412 - 1.7315\hat{u} + 0.3195\hat{u}^2, \tag{9}$$

where $\hat{P}$ is the reduced pressure and $\hat{u}$ is the reduced particle velocity. This method was selected for both its simplicity and accuracy. The right-running Hugoniot for ANFO is solved as the simultaneous solution to Eqs. (4), (6), (8), and the 1D shock jump equations. Depending on the values of α_0 and p_s, several families of Hugoniot curves may be constructed. For illustration, the crystalline AN and 50% TMD ANFO curves are shown in Fig. 6 for three different crush pressures. (Note: only porous Hugoniots are affected by the crush pressure.) The corresponding shock velocity may be determined from the intercept of the left- and right-Hugoniot curves, and then compared to the initial velocity of ~4.3 km/s measured in the small scale experiments.

Shock velocities were calculated for a broad range of α_0 and p_s values, and are shown in Fig. 7. From these calculations, shock velocity is unaffected by the crush pressure until a certain minimum value; this corresponds to the value of the resulting shock pressure, which is nominally 10 GPa for the porous Hugoniots. At 50% TMD, a crush pressure of about 12.5 GPa is required to shift the shock velocity from about 4.2 km/s to 4.3 km/s, and match the measured data. A list of all the unreacted EOS model parameters for ANFO may be found in Table II; additional discussion of the role of the unreacted EOS is given with the results section.

D. Product equation of state

A Jones-Wilkins-Lee (JWL) EOS was used to represent the detonation products of ANFO, as well as the Primasheet® 1000 booster explosive. The JWL EOS has the form[24]

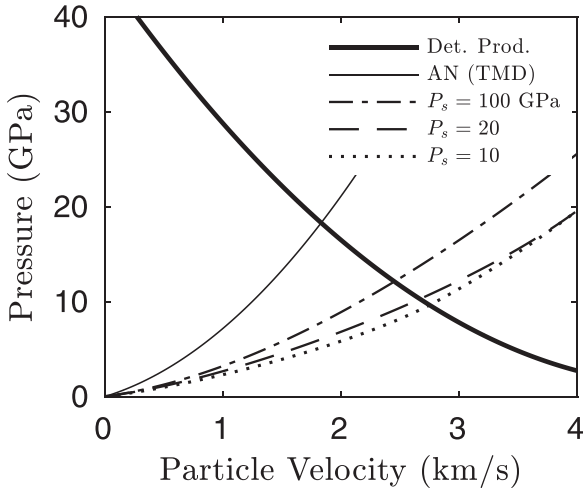

FIG. 6. Left-running Hugoniot for Primasheet® 1000; right-running Hugoniots for AN (TMD), and 50% TMD ANFO with different crush pressures.

$$p = A\left(1 - \frac{\omega}{R_1\mathbf{V}}\right)e^{-R_1\mathbf{V}} + B\left(1 - \frac{\omega}{R_2\mathbf{V}}\right)e^{-R_2\mathbf{V}} + \frac{\omega e}{v}, \quad (10)$$

where $\mathbf{V}$ stands for the relative volume (v/v_0), and A, B, R_1, R_2, and ω are the fitted constants. In this work, both TIGER[25] and CHEETAH[16] thermochemical equilibrium codes were used to determine the JWL parameters via adiabatic expansion of the CJ state. The JWL parameter values and CJ state are summarized in Table III. A composition of 63% pentaerythritol tetranitrate, 28% ethylene glycol dinitrate, and 9% acetyl tributyl citrate was assumed in TIGER to match the initial density and detonation velocity of Primasheet® 1000. The explosive booster was then modeled using a programmed burn, propagating at the calculated CJ velocity.

E. Reaction rate model

The ignition and growth reactive flow model was closed with a two-term reaction rate and set of mixture laws. A

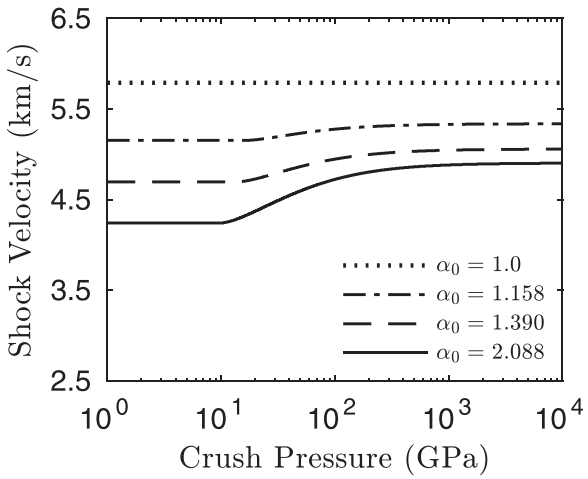

FIG. 7. Shock velocity from impedance matching as a function of crush pressure, for AN (TMD) and 90%, 75%, and 50% TMD ANFO (top to bottom).

TABLE II. Equation of state parameters used to represent the unreacted ANFO explosive.

Crystalline EOS for AN		p-α model for ANFO	
ρ_0	1.725 g/cm^3	ρ_{M0}	1.725 g/cm^3
Γ_0	1.0	ρ_0	0.826 g/cm^3
c_0	2.2 km/s	α_0	2.088
s	1.96	p_s	12.5 GPa
q	0	p_e	0

general class of pressure-dependent rate laws is given by the formula

$$\dot{\lambda} = \sum_j s_j(\lambda) r_j(p, \rho, ...), \quad (11)$$

where λ is the mass fraction of the reaction products, $s_j(\lambda)$ is a function representing the burn surface area, and $r_j(p, \rho, ...)$ is a pressure-dependent burn rate that may also be a function of density and other state variables. The rate law defined by Eq. (11) is phenomenological, and is used to describe subgrid phenomena in a continuum simulation.

The mass fraction of the reaction products is defined implicitly via the mixture law

$$V = \lambda V_{DP} + (1 - \lambda)V_{UR}, \quad (12)$$

where V_{UR}, V_{DP}, and V are the volume of the unreacted explosive, detonation products, and total volume, respectively, within a single computational cell. The solution of Eq. (12) for $\lambda = V_{DP}/V$ may be used to illustrate how different burn surface topologies provide the functional form of $s(\lambda)$. Two possibilities are hole and grain burning; a summary of the different burn surface area functions may be found in Table IV.

Following original work on ignition and growth[12,26] and to limit the number of free model parameters, the ANFO reaction rate law assumes spherical hole burning with late time grain burning behavior. It is given by the equations

$$\dot{\lambda} = I(1 - \lambda)^{2/9}\eta^4 + G(1 - \lambda)^{2/9}\lambda^{2/3}p^{0.9} \quad (13)$$

and

$$\eta = \rho/\rho_0 - 1 - a, \quad (14)$$

where I is the coefficient of ignition, G is the coefficient of growth, η is the relative compression, and a is a compression

TABLE III. Equation of state parameters for the detonation products.

Explosive	ANFO	Primasheet® 1000
A (GPa)	178.42	711.31
B (GPa)	2.85	27.83
R_1	6	5.782
R_2	2	1.941
ω	0.399	0.359
P_{CJ} (GPa)	4.37	18.52
D_{CJ} (km/s)	4.52	7.10
T_{CJ} (K)	3048	3878

TABLE IV. Summary of different burn surface area functions for the ignition and growth rate law.

$s(\lambda)$	Type
$(1-\lambda)$	Bulk reaction
$\lambda^{2/3}$	Hole burning for spherical hot spots
λ^{n}	Generalized hole burning
$(1-\lambda)^{2/3}$	Inward spherical grain burning
$(1-\lambda)^{n}$	Generalized grain burning

threshold. The ignition term is set to zero until a minimum compression value is reached (i.e., $\eta > 0$), and it is turned off when the reaction progress exceeds a certain threshold (i.e., $\lambda > \lambda_{ig}$). In contrast, the growth term is always "on" and reduces to zero when $\lambda = 0$ or $\lambda = 1$.

The exponents of the burn rate terms in Eq. (13) were also chosen to have a physical basis. It is known to a good approximation that the relative compression, η, is proportional to pressure squared; hence, the η^4 dependence predicts that ignition goes as the amount of plastic work (i.e., $\eta^4 \sim \int p^2 dt$) required for dynamic void collapse.[12] The pressure exponent of 0.9 represents a weak pressure-dependent laminar burn rate law, which was similar to other reactive flow models for non-ideal explosives.[18,27] The pressure exponent is also significant in that lower values tend to increase the non-ideal behavior.[28] Moreover, some burn rate measurements[29] have been made for ANFO up to ~100 MPa, where the pressure exponents fall between 0.8 and 1.0.

The reactive flow model was implemented in CTH,[30] a shock physics hydrocode owned by Sandia National Laboratories. CTH is used to model multidimensional, multimaterial, large deformation shock wave physics, and employs a fixed Eulerian mesh with Lagrangian and remap solution steps. A 2D cylindrical geometry was implemented having a domain of $1.25 \times 10\,\mathrm{cm}^2$; this was enlarged in width to $5 \times 10\,\mathrm{cm}^2$ for the final calculations. Mesh resolution was achieved with 65.1 μm, or 15.36 zones per mm, and two symmetry plus two zero pressure boundary conditions were used to achieve radial symmetry without recirculation zones.

It should be remarked here that all convergence studies were made on the simulated shock velocity profiles. However, the ignition and growth model is sensitive to the leading shock pressure, which in turn depends on the mesh resolution and time integration of the p-α porosity model. Future work attempting to implement this model should employ a similar mesh density (~15 zones per mm) to ensure the same reactive wave behavior.

V. RESULTS AND DISCUSSION

Four different configurations of a small scale characterization experiment for ANFO (see Table I) were analyzed and subsequently modeled using the calibrated ignition and growth parameters shown in Table V. In summary of the model calibration process, a single "goodness-of-fit" metric was introduced, based on a sum of squared errors function for the instantaneous shock velocity. The parameter sampling limits in Table V were identified with the assistance of a Latin hypercube sampling (LHS) algorithm.[31] Once these limits were established, the parameter values were fine-tuned by hand to obtain the best possible fit to the experimental data (and specifically the THK case). A comparison between the experimental and simulated shock velocities is shown in Fig. 8, where the experimental data is averaged and de-sampled for improved visualization.

TABLE V. Sampling limits and calibrated ignition and growth model parameters. All units are in cgs.

Parameter	Low	High	Fit
I	1×10^5	1×10^8	1×10^7
a	0	0.4	0.2
λ_{ig}	0.01	1	0.3
G	0	3×10^{-4}	0.6×10^{-4}

It is likely that the shock velocity depends on both the unreacted EOS, as well as the ignition and growth parameters for ANFO. Early attempts to find a common set of ignition and growth parameters were largely unsuccessful—agreement could only be achieved for the PVC and THK cases individually. However, the early calibration attempts had assumed a default crush pressure of 100 MPa. The analysis of left- and right-running Hugoniot curves, which determined the crush pressure to be 12.5 GPa, was significant in at least two ways. First, the new crush pressure forced all velocity curves to pass through the experimentally determined shock velocity at $x = 0$, and second, the SM and THN simulations showed compression waves that persisted over a greater length of the samples. (Note in Fig. 8 the model curves are suppressed when it is no longer possible to distinguish the front of the compression wave.) The unusually large value of 12.5 GPa for the crush pressure might also suggest deficiencies in the unreacted EOS; for example, the accuracy of the Hugoniot data or the time dependency of the p-α porosity model.

The simulations also provide a wealth of information beyond the shock wave velocity. Using the calibrated

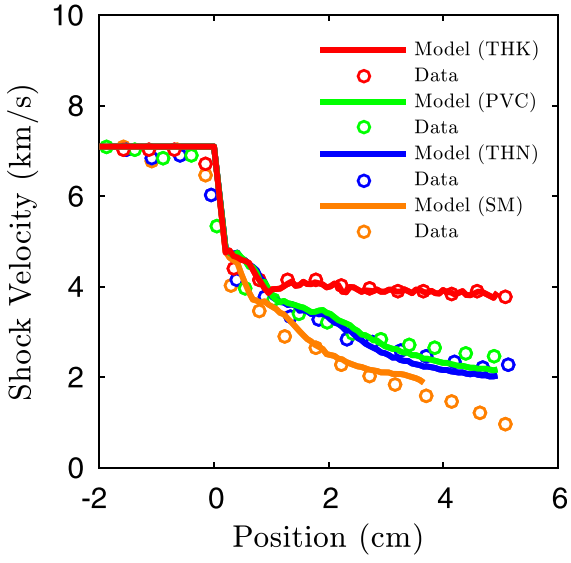

FIG. 8. Model shock velocity together with the MI data (averaged and de-sampled for visualization).

parameters, it is possible to visualize the pressure levels inside the experiments, as well as the extent of reaction. Pressure and reaction contours are shown in Figs. 9 and 10, respectively, for $t = 7$, 11, 15, and 19 μs. Although the computational domain encompasses the outer charge radius, the geometry is clipped at $r = 1.25$ cm for improved visualization. One of the most intriguing aspects of the pressure contours in Fig. 9 is the shape of the pressure waves in the confiner materials. Specifically, the selection of either a high sound speed 304 stainless steel ($\sim$5 km/s) or low sound speed PVC ($\sim$2 km/s) determines whether or not the pressure waves outrun the reaction zone (THK) or trail behind it (PVC).

Also visible in Fig. 9 are regions of negative pressure, where the material is in a state of extreme tension (or spall). This occurs in the THK case when release waves arrive from the outer edges of the charge. As the stainless steel walls release, they are forced to expand beyond their original (uncompressed) density state. Spallation is also observed for the THN and SM simulations inside the ANFO samples; however, this condition is less physical. It occurs when the reactive waves transition from supersonic to subsonic deflagration, at which time the combustion products have a greater tendency to expand. Unfortunately, the unreacted EOS is artificially stiff due to the Mie-Gruneisen assumption, and it cannot expand beyond the original density without going into tension. From these observations, it is more desirable to design the small scale experiments with heavy confinement, yielding as much pressure support as is possible. This condition is also closer to the detonation regime, and seems to have the greatest applicability for calibrating the parameters of an ignition and growth reaction rate law.

The reaction contours in Fig. 10 are also intriguing, as the reaction front stalls in every simulation except for the THK geometry. Because the reaction progress variable is a weighted average between the reactant and product EOS, it is clear that the late time behavior of the SM, THN, and PVC simulations must be dominated by the unreacted EOS. This observation is fundamental to answering the question of whether the small scale MI data is even relevant to calibrating a reactive burn model. Interestingly, the shock velocity in the THK configuration is much higher than the other data,

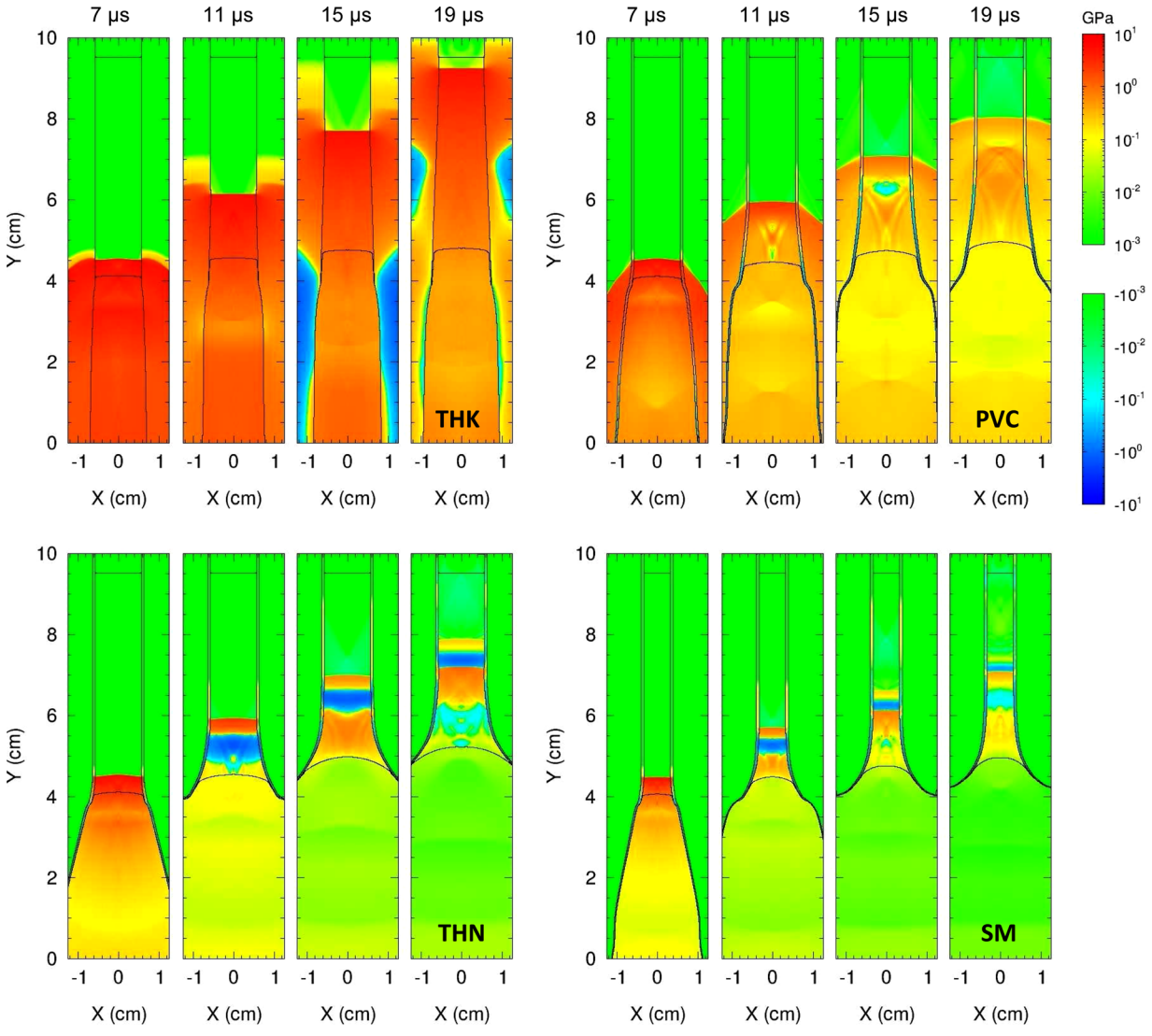

FIG. 9. Pressure contours for the different ANFO charge geometries at $t = 7$, 11, 15, and 19 μs. (Negative pressures correspond to areas where spallation occurs.)

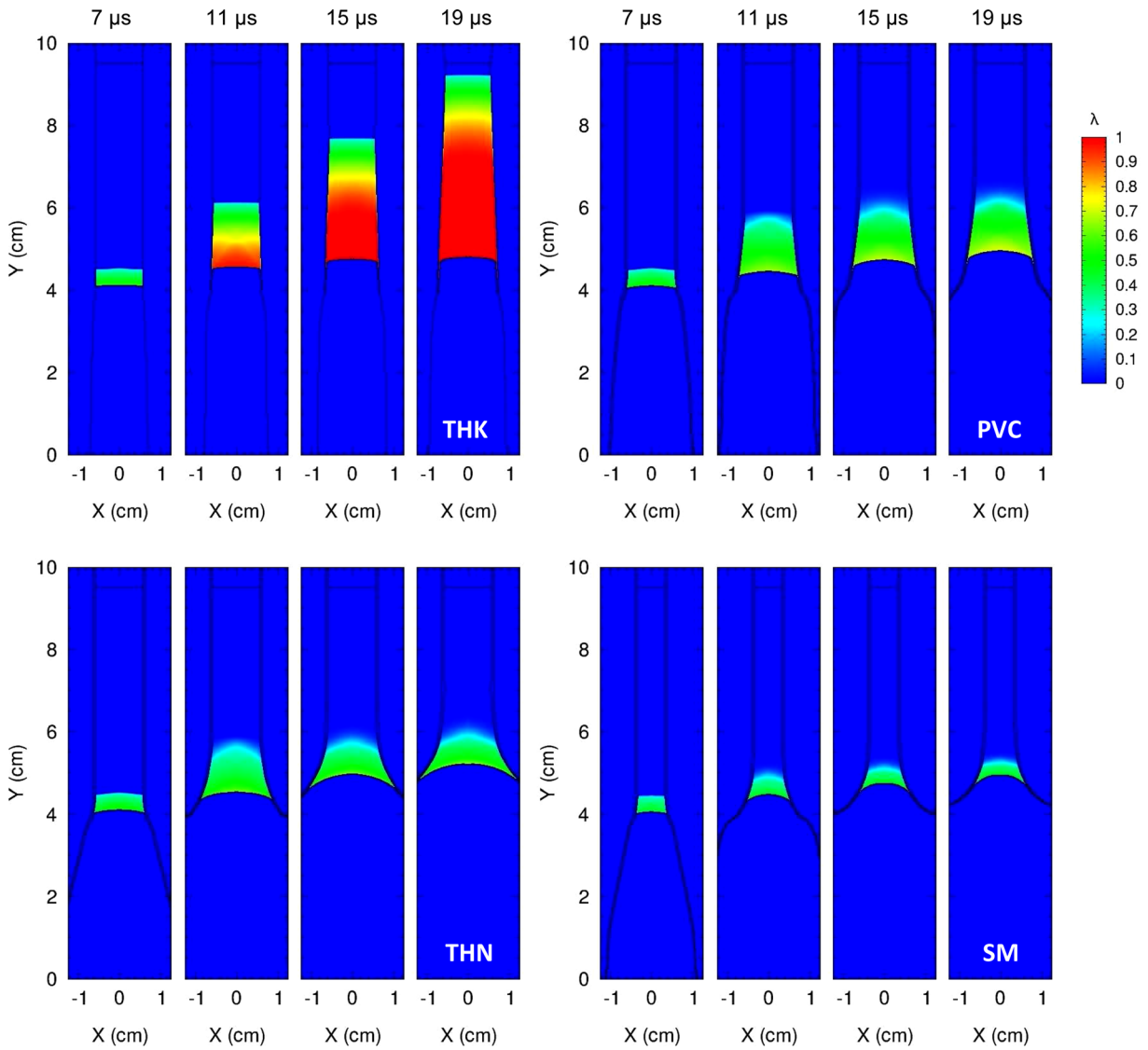

FIG. 10. Extent of reaction contours for the different ANFO charge geometries at $t = 7$, 11, 15, and 19 μs.

and the reaction front is propagated until the end of the sample. For the THK case, the ignition and growth reaction rate law is successful in slowly releasing the chemical energy 1–2 cm behind the leading shock wave, and is able to match the experimental data exactly. (The slow release of chemical energy is most likely attributable to the pressure exponent of 0.9 in the growth term, which is known to spread out the reaction zone.) The release of chemical energy is necessary to prevent rapid deceleration of the shock waves in any of the simulations. Ultimately, the insight gained from visualization of both the pressure and reaction contours supports the calibration of an ignition and growth model when the ANFO samples are highly confined.

Finally, from the analysis and simulation of the small scale experiments, it is still unknown if any aspect of the velocity curves are related to a steady-state detonation velocity. The initial shock velocity at $x = 0$ is likely a result from shock impedance matching, and afterwards the shock decelerates depending on the level of reaction. If the shock velocity were to asymptote to a steady value (similar to the THK case), this may correspond to a large scale detonation velocity. However, the CJ velocity of non-ideal explosives cannot be determined, in general, without large scale testing. The detonation velocities predicted in Table III from TIGER and CHEETAH assumed chemical equilibrium. Moreover, the JWL EOS is calculated to pass through the CJ state, so that the reactive flow model may asymptote to this value for complete reaction. Incomplete reaction will prevent the full detonation energy from being deposited into the flow. Hence, a velocity lower than that predicted by CJ theory may be calculated simply by adjusting the parameters of ignition and growth.

Future work should be considered to improve the reactive flow model for ANFO. Additional experiments to vary the explosive packing density and initiating shock pressure would better inform the roles of the unreacted EOS and the ignition and growth reaction rate. If different combinations of pressure and density were found to shift the location of the shock velocity at $x = 0$, it may be possible to reconstruct the porous Hugoniot for ANFO directly. Furthermore, larger sample diameters should be considered, in the hopes that the shock velocity achieves a steady value; this value may or

may not be directly related to a large diameter detonation velocity. Testing at larger diameters has one additional benefit that the reactive flow model may be assessed for an incremental scale up. Finally, other non-ideal explosives of interest should be considered, to see whether the behavior is similar to or different than the baseline ANFO samples. This is especially relevant to other varieties of ANFO which are more sensitive than the baseline formulation.[32]

While much additional work has been proposed to better understand the combined chemical-mechanical response, the simulation results are sufficient to answer the fundamental question posed at the beginning. A reactive flow model, such as ignition and growth, is relevant for simulating the small scale data on non-ideal explosives when the samples are highly confined and overdriven. This result will help to advance the current state of the art for small scale screening, characterization, and modeling of non-ideal explosives.

VI. CONCLUSIONS

Small scale characterization experiments requiring only 1–5 g of material were demonstrated for a baseline ANFO explosive, and then simulated using the shock physics hydrocode CTH. No previous work has shown whether any useful or meaningful result may be obtained from small scale experiments applied to non-ideal explosives; yet, there exists a strong need for these types of studies to adequately survey the wide parameter space in sample composition, density, and microstructure. The velocity data obtained from MI corresponds to transient, overdriven shock waves that are well below the CJ value. For the first time, it is shown that a reactive flow model based on the theory of ignition and growth is relevant for simulating the experiments when the samples are highly confined. Specifically, the velocity data was matched for a 7.6 cm dia. stainless steel cylinder having a 1.1 cm bore filled with the baseline explosive.

These simulations also provide a wealth of information beyond the shock wave velocity, including detailed pressure and reaction contours. From this information, it is observed that the reaction front stalls in three of the four geometries tested, as the reaction transitions from supersonic to subsonic deflagration. Only the heaviest stainless steel confinement supports pressures closer to the detonation regime, where a thick reaction zone 1–2 cm long is established. Ultimately, the measured shock velocity is a complex result of both the unreacted EOS and reaction rate for ANFO. Other studies should consider new experiments to gain greater insight into the shock velocity data. Some of these experiments must include varying the pressing density, sample diameter, and initiating shock pressure, as well as testing additional non-ideal explosive compositions.

ACKNOWLEDGMENTS

This material is based upon work supported by the U.S. Department of Homeland Security, Science and Technology Directorate, Office of University Programs, under Grant Award No. 2013-ST-061-ED0001. The views and conclusions contained in this document are those of the authors and should not be interpreted as necessarily representing the official policies, either expressed or implied, of the U.S. Department of Homeland Security.

[1]S. Schoch, N. Nikiforakis, and B. J. Lee, "The propagation of detonation waves in non-ideal condensed-phase explosives confined by high sound-speed materials," Phys. Fluids **25**, 086102 (2013).
[2]R. S. Janesheski, L. J. Groven, and S. F. Son, "Detonation failure characterization of homemade explosives," Propellants Explos. Pyrotech. **39**, 609–616 (2014).
[3]S. Nie, J. Deng, and A. Persson, "The dead-pressing phenomenon in an ANFO explosive," Propellants Explos. Pyrotech. **18**, 73–76 (1993).
[4]B. Zygmunt and D. Buczkowski, "Influence of ammonium nitrate prills' properties on detonation velocity of ANFO," Propellants Explos. Pyrotech. **32**, 411–414 (2007).
[5]A. Miyake, K. Takahara, T. Ogawa, Y. Ogata, Y. Wada, and H. Arai, "Influence of physical properties of ammonium nitrate on the detonation behavior of ANFO," J. Loss Prev. Process **14**, 533–538 (2001).
[6]R. A. Catanach and L. G. Hill, "Diameter effect curve and detonation front curvature measurements for ANFO," in *Proceedings of the Twelfth American Physical Society Topical Conference on Shock Compression of Condensed Matter* (IOP Institute of Physics Publishing, Ltd., 2002), Vol. 2, pp. 906–909.
[7]W. W. Wood and J. G. Kirkwood, "Diameter effect in condensed explosives: The relation between velocity and radius of curvature of the detonation wave," J. Chem. Phys. **22**, 1920–1924 (1954).
[8]S. I. Jackson, C. B. Kiyanda, and M. Short, "Experimental observations of detonation in ammonium-nitrate-fuel-oil (ANFO) surrounded by a high-sound-speed, shockless, aluminum confiner," Proc. Combust. Inst. **33**, 2219–2226 (2011).
[9]J. Kennedy, I. Plaksin, K. Thomas, E. Martin, K. Y. Lee, A. Akinci, B. Asay, J. Campos, and J. Direito, "Instrumented Floret tests of detonation spreading," in *Proceedings of the Thirteenth American Physical Society Topical Conference on Shock Compression of Condensed Matter* (AIP Publishing, 2004), Vol. 706, pp. 1500–1504.
[10]L. G. Hill, W. L. Seitz, C. A. Forest, and H. H. Harry, "High explosive corner turning performance and the LANL mushroom test," in Proceedings of *the Tenth American Physical Society Topical Conference on Shock Compression of Condensed Matter* (AIP Publishing, 1998), Vol. 429, pp. 751–754.
[11]T. D. Tran, P. F. Pagoria, D. M. Hoffman, B. Cunningham, R. L. Simpson, R. S. Lee, and J. L. Cutting, "Small–scale safety and performance characterization of new plastic bonded explosives containing llm-105," in *Proceedings of the 12th International Detonation Symposium* (2002), pp. 440–447.
[12]E. L. Lee and C. M. Tarver, "Phenomenological model of shock initiation in heterogeneous explosives," Phys. Fluids **23**, 2362–2372 (1980).
[13]D. E. Kittell, J. O. Mares, and S. F. Son, "Using time-frequency analysis to determine time-resolved detonation velocity with microwave interferometry," Rev. Sci. Instrum. **86**, 044705 (2015).
[14]A. D. Krall, B. C. Glancy, and H. W. Sandusky, "Microwave interferometry of shock waves. I. Unreacting porous media," J. Appl. Phys. **74**, 6322–6327 (1993).
[15]B. C. Glancy, H. W. Sandusky, and A. D. Krall, "Microwave interferometry of shock waves. II. Reacting porous media," J. Appl. Phys. **74**, 6328–6334 (1993).
[16]L. E. Fried, W. M. Howard, and P. C. Souers, "Cheetah 6.0 User's Manual," Technical Report No. LLNL-SM-416166 (Lawrence Livermore National Laboratory, Livermore, CA, USA, 2010).
[17]E. Grüneisen, *Handbuch der Physik* (Verlag Julius Springer, Berlin, 1926), Vol. 10, pp. 1–59.
[18]M. A. Price and A. H. Ghee, "Modeling for detonation and energy release from peroxides and non-ideal improvised explosives," Cent. Eur. J. Energetic Mater. **6**, 239–254 (2009), ISSN 1733-7178.
[19]P. W. Cooper, *Explosives Engineering* (Wiley-VCH, New York, 1996).
[20]A. N. Dremin, K. K. Shvedov, and O. S. Avdonin, "Shock compressibility and temperature of certain explosives in the porous state," Combust. Explos. Shock **6**, 449–455 (1970).
[21]W. Herrmann, "Constitutive equation for the dynamic compression of ductile porous materials," J. Appl. Phys. **40**, 2490–2499 (1969).
[22]M. M. Carroll and A. C. Holt, "Static and dynamic pore-collapse relations for ductile porous materials," J. Appl. Phys. **43**, 1626–1636 (1972).
[23]A. W. Campbell, W. C. Davis, J. B. Ramsay, and J. R. Travis, "Shock initiation of solid explosives," Phys. Fluids **4**, 511–521 (1961).

[24]E. L. Lee, H. C. Horning, and J. W. Kury, "Adiabatic expansion of high explosive detonation products," Technical Report No. UCRL-50422 (Lawrence Livermore Radiation Laboratory, University of California, 1968).
[25]M. L. Hobbs and M. R. Baer, "Nonideal thermoequilibrium calculations using a large product species data base," Shock Waves **2**, 177–187 (1992).
[26]C. M. Tarver and J. O. Hallquist, "Modeling two-dimensional shock initiation and detonation wave phenomena in PBX 9404 and LX-17," in *Proceedings of the 7th International Detonation Symposium* (1981), pp. 488–497.
[27]H. R. James, B. D. Lambourn, C. A. Handley, N. J. Whitworth, H. N. Angseesing, P. J. Haskins, M. D. Cook, A. D. Wood, R. I. Briggs, and P. R. Ottley, "An investigation of the detonation characteristics of some non-ideal explosive compositions based upon ammonium nitrate," in *Proceedings of the 13th International Detonation Symposium* (2006), pp. 110–120.
[28]P. J. Haskins and M. D. Cook, "Detonation failure in ideal and non-ideal explosives," in *Proceedings of the 15th American Physical Society Topical Conference on Shock Compression of Condensed Matter* (AIP Publishing, 2007), pp. 881–884.
[29]V. P. Sinditskii, V. Y. Egorshev, A. I. Levshenkov, and V. V. Serushkin, "Ammonium nitrate: combustion mechanism and the role of additives," Propellants Explos. Pyrotech. **30**, 269–280 (2005).
[30]J. M. McGlaun and S. L. Thompson, "CTH: A three-dimensional shock wave physics code," Int. J. Impact Eng. **10**, 351–360 (1990).
[31]L. P. Swiler and G. D. Wyss, "A user's guide to Sandia's Latin hypercube sampling software: LHS UNIX library and standalone version," Technical Report No. SAND04-2439 (Sandia National Laboratories, 2004).
[32]B. Zygmunt and D. Buczkowski, "Agriculture grade ammonium nitrate as the basic ingredient of massive explosive charges," Propellants Explos. Pyrotech. **37**, 685–690 (2012).